**Geomechanics and Engineering**, *Vol. 41, No. 3 (2025) 351-364*
https://doi.org/10.12989/gae.2025.41.3.351


# Three-dimensional rock mass collapse mechanism caused by a hidden spherical karst cave above a deep rectangular cavern

Fu Huang[1a], Min Zhang*[1], Tonghua Ling[1b] and Xiaoli Yang[2c]

[1]*School of Civil and Environmental Engineering, Changsha University of Science and Technology, Changsha, Hunan, China*
[2]*School of Civil Engineering, Central South University, Changsha, Hunan, China*

(*Received April 19, 2023, Revised March 31, 2025, Accepted April 13, 2025*)

**Abstract.** When a tunnel or underground cavern is excavated in a karst region, a hidden karst cave may occur close to the planned tunnel or underground cavern, which may potential to cause the collapse damage of the surrounding rock during the excavation. Since many previous studies on this issue are carried out based on a two-dimensional model, the three-dimensional collapse mechanism for the surrounding rock is not well investigated. In this study, a three-dimensional approach to determine the rock mass collapse range caused by a hidden spherical karst cave above a rectangular cavern is developed. Based on the rock mass collapse characteristics caused by a hidden karst cave above the deep cavern roof, a three-dimensional rock mass collapse mechanism is established, and the collapse surface equation is derived from the variational approach in combination with the upper bound theorem. By utilizing the aforementioned collapse surface equation, three-dimensional collapse surfaces influenced with varying parameters are depicted. Moreover, a numerical model that describes a spherical karst cave occurring above a rectangular cavern is established by employing three-dimensional numerical software, and the numerical solution of the collapse surface is obtained, which is represented by contour of maximum shear strain increment. By comparing the collapse surface derived from the latter computation and that attained from numerical simulation, the validity of the proposed approach is demonstrated.

**Keywords:** collapse volume; difference method; three-dimensional collapse surface; three-dimensional failure mechanism; variational approach

## 1. Introduction

Karst is a common landform that is widely distributed in southwestern China. Due to the widespread and stochastic distribution of karst caves in karst regions, existing surveying technologies face significant challenges in accurately determining their spatial coordinates and dimensions. Consequently, during the construction of tunnels or underground caverns in such areas, these caves may unpredictably emerge within or adjacent to the excavation boundaries of engineered structures. Currently, most of the deep buried underground structures are excavated by the drilling and blasting method. The shock wave produced by blasting would disturb the stress equilibrium state of the rock mass around the underground structures. Assuming a karst cave occurs near a planned underground structure, the blast vibrations may give rise to the collapse of the rock pillars between the karst cave and the underground structure. In particular, if a large filler amount is present in the karst cave, the filler material may break through the rock pillars and rush into the underground structure due to the very high filler pressure, which would enlarge the collapse region of the surrounding rock mass. Since rock mass collapses caused by karst caves during underground excavation occur instantaneously, they pose significant safety risks to construction workers. Accordingly, it is essential to investigate the rock mass collapse position and range during underground structure excavation in a karst region. Based on the rock mass collapse position and range, engineers can establish the optimal support scheme to avoid the occurrence of rock mass collapse resulted from such a cave.

Presently, numerous scholars have studied this issue and obtained several achievements. Considering that the failure of the pillar between the karst cave and a coal mine would cause groundwater inrush during the coal mining process, Ma *et al*. (2016) constructed a numerical model to investigate the mining influence on the risk of groundwater inrush induced by the collapse of the penetrated karst pillar. Using this model, Ma *et al*. (2016) obtained the destruction zone in the penetrated karst collapse pillar. Thus, when tunnel excavations are conducted in a karst region, groundwater can flow into the tunnel through potential water channels and can cause an engineering accident. Finding Ground Penetrating Radar (GPR) can discriminate the filling materials in a karst cave effectively, Caselle *et al*. (2020) applied the GPR technique to identify the major risk

*Corresponding author, Ph.D. Student
E-mail: zm0706@stu.csust.edu.cn
[a]Professor
E-mail: hfcsu0001@163.com
[b]Professor
E-mail: lingtonghua@163.com
[c]Professor
E-mail: hfzndx2002@aliyun.com

**Copyright © 2025 Techno-Press, Ltd.**

ISSN: 2005-307X (Print), 2092-6219 (Online)

factors associated with karst phenomenon during underground excavations. To guarantee tunnels crossing through karst regions safely, Garasic and Garasic (2016) summarized some unusual engineering constructions which are applied in a series of tunnels constructed in Dinaric Karst of Croatia. Because the existence of karst caves constitutes a great threat to underground construction, Li *et al*. (2019) put up a possible prediction technique to determine the location of a hidden karst cave through displacement monitoring method. In addition, this technique was validated by comparing the displacement laws of the tunnel arch achieved from numerical simulation with those predicted by the proposed technique. The collapse of a rock pillar between a tunnel and a karst cave can potentially lead to the hazardous inflow of water and mud into the tunnel. Therefore, the investigation of the minimum safe thickness of the rock pillar has been subject to scholarly attention. On the basis of the elastic mechanics method, Xu *et al*. (2018) built mechanical models of karst caves situated above, below and adjacent to an excavated tunnel and derived semi analytical solutions for determining the minimum safe thickness of the rock pillar. Subsequently, Wu *et al*. (2019) calculated the minimum safe thickness of the rock pillar located between the tunnel face and karst cave to prevent ingress of water and mud following seismic activity. The mechanical models proposed by Wu *et al*. (2019) are applied to actual tunnels excavated in karst regions, and the validity of the theoretical calculation results was also proved. Moreover, Zhang and Yang (2019) established a new 3D failure mechanism that reflects active and passive failure patterns of the rock mass caused by a water-filled karst cave beneath the tunnel floor. Based on this new 3D failure mechanism, the analytical expressions of the rock mass failure are derived, and the effect of various rock parameters on failure surface is obtained by parameter sensitivity analysis.

The existing literature has demonstrated that the collapse of the rock pillar linking underground structures to karst caves is common during tunnel excavation in karst areas, therefore, investigators intend to find a way to determine the collapse position and range of the rock stratum. By utilizing the limit analysis theorem and the variational approach, Fraldi and Guarracino (2009) proposed a new method to obtain the analytical expression of the falling area of the surrounding rock above a deep rectangular cavern. For the reason that Fraldi and Guarracino (2009) used arbitrary curves to characterize the rock mass failure mechanism, it was not confined to a predetermined curve type (such as a parabola or a hyperbola). Consequently, the final collapse area predicted by their method closely matches the actual collapse area observed in the real-world project. Subsequently, Fraldi and Guarracino (2010) employed this method to study the geometric characteristics of collapse surface of the rock mass above tunnels with arbitrary profiles. Considering the advantage of this approach, investigators have also used it to study the rock mass collapse mechanism for tunnel roof and tunnel face (Yang and Huang 2013, Qin *et al*. 2015a, Qin *et al*. 2015b, Yang and Li 2016, Guan *et al*. 2017, Li *et al*. 2017, Yang and Zhang 2017, Zhang *et al*. 2017, Wang *et al*. 2019, Huang *et al*. 2021). Finding existing studies of tunnel excavation mainly focused on the failure mechanism of rock mass, Park and Michalowski (2019) defined stability number, support pressure, and factor of safety as three indexes to assessing the stability of the surrounding rock at the top of the deep tunnels. By using a two-dimensional failure mechanism, Park and Michalowski (2019) calculated the values of these three stability indexes within the domain of the kinematic approach of limit analysis and obtained the rules of stability for tunnel roof varying with these stability measures. Immediately after, Park and Michalowski (2020) developed their method to assess the stability of the roof in circular cross-section tunnel by extending the two-dimensional failure mechanism into three dimensions.

As the methodology presented by Fraldi and Guarracino (2009) can determine the rock mass collapse range around a tunnel, investigators have utilized this methodology to examine the stability of the rock stratum between a karst cave and a tunnel. To study the collapse mode of the rock stratum located between a tunnel face and a water-bearing cave ahead of the tunnel, Yang and Zhang (2016) formed an upper bound mechanism based on the failure features of the rock stratum induced by a water-bearing karst cave ahead of the tunnel face. Using this failure mechanism, Yang and Zhang (2016) provided an equation of the minimum safe thickness of the rock stratum located between the tunnel face and the karst cave ahead of the tunnel. In order to predict the rock mass collapse range where a karst cave exists beneath a motorway tunnel, in accordance with the methodology proposed by Fraldi and Guarracino (2009), Huang *et al*. (2017) investigated the two-dimensional collapse surface corresponding to rock mass failure caused by a karst cave. Subsequently, Yang *et al*. (2017) studied the tunnel floor collapse range in a karst terrain by utilizing the functional catastrophe theory. Afterwards, based on the failure features of the rock pillar between the base of a deep buried tunnel and a water-filled cave roof, Zhang (2019) established collapse and blow-out failure mechanisms. Using these mechanisms, Zhang (2019) derived the failure surfaces of the rock stratum between the base of a deep buried tunnel and the ceiling of a water-filled cavern within the domain of the upper bound theorem and the functional catastrophe theory. Furthermore, some scholars have conducted a series of studies on rock mass stability in karst tunnels, yielding significant findings (Wu *et al*. 2022, He *et al*. 2023, Xiao *et al*. 2024).

Although the solutions presented by these investigators provided effective methods to investigate the rock mass falling range caused by a karst cavern during tunnel excavation, the failure mechanisms reported in the literature are two-dimensional. However, rock mass deterioration in an actual project is a three-dimensional evolutionary process, and the rock mass collapse range results derived from two-dimensional failure mechanisms are underestimated (Yang and Huang 2013). If the construction scheme is based on the results provided by a two-dimensional failure mechanism, a high risk exists in the underground structure excavation process. Therefore, if the hree-dimensional size of the rock mass collapse block can

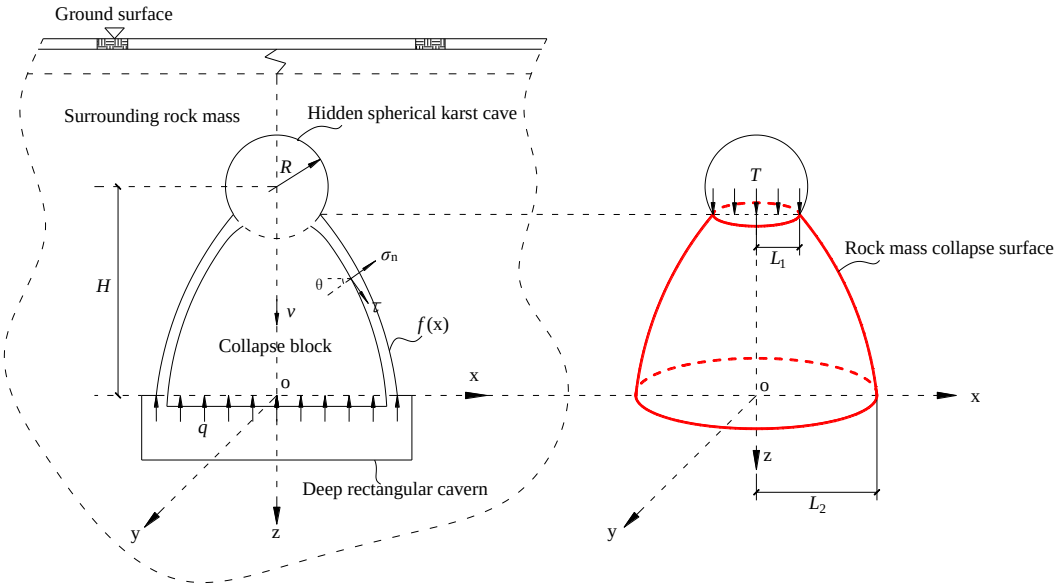


Fig. 1 The 3D failure mechanism of the rock mass caused by a hidden spherical karst cave above a deep rectangular cavern

be calculated, engineers can determine the optimal construction scheme to decrease the collapse risk during underground structure excavation in karst areas.

In view of the situation mentioned above, this paper developed a three-dimensional approach to find out the rock mass collapse range caused by a hidden spherical karst cave above the ceiling of a deep rectangular cavern. By analyzing the collapse characteristics of the rock mass between a spherical karst cave and a rectangular cavern, a three-dimensional failure mechanism is established. Utilizing this mechanism, the analytical equation of the collapse block is obtained within the domain of the kinematic method of limit analysis theory in line with the variational approach. The three-dimensional collapse block shape and range are plotted based on the collapse block equation. To verify the validity of this method, the analytical solution presented in this paper is used to make a comparison with the result generated by numerical simulation. The research presented here has the potential to assist engineers in predicting the rock mass collapse dimensions and positions resulting from a hidden karst cave during the construction of deep underground structures.

## 2. Three-dimensional failure mechanism of a rectangular cavern caused by a hidden spherical karst cave

A hidden karst cave tends to cause rock mass collapse in underground structure excavation, especially in cases where a karst cave exists directly above the ceiling of an underground structure. When explosive vibrations are transferred from the underground structure to the karst cave, the rock stratum may fall due to the rock mass gravity and filler pressure. Yang and Huang (2013) established a three-dimensional failure mechanism to describe the collapse characteristics of the rock mass above the ceiling of a cavern. However, karst caves are not considered in their ailure mechanism, and the effect of a karst cave on the collapse block range can therefore not be determined. Thus, taking the failure mechanism produced by Yang and Huang (2013) as a reference, a new 3D failure mechanism that describes the rock mass failure characteristics caused by a spherical karst cave above the ceiling of a deep rectangular cavern was established. As demonstrated in Fig. , a spherical karst cave of radius R rests atop the roof of a rectangular cavern. The distance between the center of the sphere and the rectangular roof is denoted as *H*. Two arbitrary curves $f(x)$, symmetrically aligned, stretch from the roof of the cavern all the way down to the base of the karst cave. If the curve undergoes a 360-degree rotation around the Z-axis, it generates a 3D rotational body. Due to the effects of the blast vibrations and filler pressure in the karst cave, minor sliding would occur along the interface between the 3D rotational body and the rest of the surrounding rock, which causes a velocity discontinuity along the interface. Thus, the interface and curve $f(x)$ can be referred to as the velocity discontinuity surface and velocity discontinuity curve, respectively. Since the 3D rotational body detaches from the surrounding rock mass, it is considered as the collapse block, with the interface between it and the remaining rock mass constituting the collapse surface. This paper focuses on analyzing the shape and range of this collapse surface.

Furthermore, because the collapse surface is constituted by the arbitrary curve $f(x)$, the collapse surface is also an arbitrary surface. An arbitrary surface indicates that the collapse surface shape is not known a priori, and no assumption (such as a cone or a paraboloid) is required in the calculation process. As the final solution of the collapse surface comes from the optimization calculation, the collapse surface shape obtained by the proposed method may approximate the collapse surface shape obtained in numerical simulation or examined in actual engineering.

## 3. Calculation process of the three-dimensional collapse surface caused by a hidden spherical karst cave above a cavern roof

### *3.1 The calculation of the analytical equation for the 3D collapse surface*

As previously stated, the presence of filler pressure may cause slight sliding to occur along the interface between the collapse block and the rest of the surrounding rock mass. Thus, friction is produced by the relative sliding along the interface. Due to the friction, energy dissipation occurs on the collapse surface. As highlighted by Chen (1975), the rate at which energy dissipates for any given point on the collapse surface can be computed using the relation between the plastic stress/strain rate. Furthermore, the stress/strain rate relation is derived by fulfilling the normality condition that corresponds to a yield function.

The Hoek-Brown (H-B) failure criterion is practical for assessing the strength of a rock mass, whether it is composed of closely interlocked units or of very poor quality (Lyu *et al*. 2019, Xiao *et al*. 2019, Peng *et al*. 2019, Fraldi *et al*. 2019). This paper seeks to investigate the collapse of rock mass caused by a spherical karst cave during deep cavern excavation works. To calculate the dissipation of energy along the collapse surface, the H-B failure criterion is employed. Assuming the plastic potential, $\Omega$ , to be coincident with the H-B yield surface, the former is established as follows

$$\Omega = \tau - A\sigma_{ci}\left(\frac{\sigma_n - \sigma_{tm}}{\sigma_{ci}}\right)^B \tag{1}$$

where $\tau$ and $\sigma_n$ represent normal and shear stresses, respectively, $A$ and $B$ stand for material constants, and $\sigma_{ci}$ denotes the uniaxial compressive strength of the rock mass. In addition, $\sigma_{tm}$ indicates the rock mass's tensile strength.

Fraldi and Guarracino (2009) formulated the energy dissipation rate for any given point positioned on the velocity discontinuity curve, represented by the following equation

$$\begin{aligned} D &= (\sigma_n \varepsilon_n + \tau\gamma_n)t \\ &= \left\{\sigma_{ci}\left[ABf'(x)\right]^{\frac{1}{1-B}}\left(1-B^{-1}\right)-\sigma_{tm}\right\}\frac{v}{\sqrt{1+f'(x)^2}} \end{aligned} \tag{2}$$

where $f(x)$ corresponds to the equation of the velocity discontinuity curve, $f'(x)$ refers to the first derivative of $f(x)$, $\varepsilon_n$ and $\gamma_n$ characterize the normal and shear plastics train rates, respectively, $v$ is the velocity vector of the collapse block and $t$ is the thickness of the collapse surface at the limit state. Because energy dissipation happens directly along the whole collapse surface, the energy dissipation rate in this failure mechanism is derived from integral calculation.

$$P_D = 2\pi\int_{L_1}^{L_2}\left\{\sigma_{ci}[ABf'(x)]^{\frac{1}{1-B}}(1-B^{-1})-\sigma_{tm}\right\}xv\,dx \tag{3}$$

where $L_1$ and $L_2$ are the radii of the top and bottom circular surfaces, respectively, of the collapse block. In addition, the external work rate is produced by the external loads, encompassing the self-weight of the collapse block, the pressure of fill material within the spherical karst cave and the supporting pressure acting on the deep cavern roof. The work rate generated by the self-weight can be defined as

$$P_\gamma = \pi\gamma v\left[\int_{L_2}^{L_1} x^2 f'(x)\mathrm{d}x - \frac{1}{3}\left(R-\sqrt{R^2-L_1^2}\right)^2\left(2R+\sqrt{R^2-L_1^2}\right)\right] \tag{4}$$

The unit weight of the rock mass is represented by $\lambda$ . And the filler pressure's work rate is calculated based on

$$P_T = 2\pi R\left(R-\sqrt{R^2-L_1^2}\right)Tv \tag{5}$$

where $T$ refers to the filler pressure within the spherical karst cave. Besides, the work rate at which the supporting pressure operates can be characterized as

$$P_q = \pi L_2^2 qv\cos\pi \tag{6}$$

where $q$ is the supporting pressure acting on the cavern ceiling. The upper bound theorem of limit analysis emphasizes that the rock mass collapse surface at the limit state can be determined by the relation between the rates of external work and internal dissipation. Therefore, an objective equation $\xi\left[f(x), f'(x), x\right]$ , which is the difference between the rates of internal dissipation and external work, reflects this relation. The objective equation $\xi\left[f(x), f'(x), x\right]$ is given as

$$\xi\left[f(x), f'(x), x\right] = P_D - P_\gamma - P_T - P_q \tag{7}$$

Combining Eqs. (3)-(6), then substituting the result into Eq. (7) yields

$$\begin{aligned} \xi = {} & 2\pi\int_{L_1}^{L_2}\psi\left[f(x), f'(x), x\right]v\,\mathrm{d}x \\ & + \frac{\pi\gamma v}{3}\left(R-\sqrt{R^2-L_1^2}\right)^2\left(2R+\sqrt{R^2-L_1^2}\right) \\ & - 2\pi R\left(R-\sqrt{R^2-L_1^2}\right)Tv + \pi L_2{}^2 qv \end{aligned} \tag{8}$$

whereas denoting $\psi\left[f(x), f'(x), x\right]$ as

$$\begin{aligned} \psi\left[f(x), f'(x), x\right] = {} & \left\{\sigma_{ci}[ABf'(x)]^{\frac{1}{1-B}}\left(1-B^{-1}\right)-\sigma_{tm}\right\}x \\ & + \frac{\gamma}{2}x^2 f'(x) \end{aligned} \tag{9}$$

Eq. (9) indicates that there are two independent variables, $x$ and $f'(x)$, in $\psi$ . However, the variable $f'(x)$ itself is also an unknown function. Thus, $\psi$ can be regarded as a functional. The upper bound theorem emphasizes that the real upper bound solution can be calculated by determining the critical values of the variables that either minimize or maximize the objective function numerically or analytically. Moreover, Eq. (8) reveals that the objective function $\xi$ is determined by the functional $\psi$ . Therefore, if there exists an equation $f(x)$, which can

minimize or maximize the functional $\psi$, the equation $f(x)$ is the desired upper bound solution. To determine the equation $f(x)$ that enables the functional $\psi$ to reach its extremum, the variational approach is adopted here. Because $\psi$ is a functional in the simplest form, according to the variational principle, when $\psi$ reaches its extremum, the necessary condition illustrated as follows should be satisfied:

$$\frac{\partial \psi}{\partial f(x)} - \frac{\mathrm{d}}{\mathrm{d}x}\left[\frac{\partial \psi}{\partial f'(x)}\right] = 0 \tag{10}$$

Substituting Eq. (9) into Eq. (10), a nonlinear second-order homogeneous differential equation is calculated as follows

$$\begin{aligned} &\gamma x - \frac{1}{B}\sigma_{ci}(AB)^{\frac{1}{1-B}}[f'(x)]^{\frac{B}{1-B}} \\ &-\frac{1}{1-B}\sigma_{ci}(AB)^{\frac{1}{1-B}}[f'(x)]^{\frac{2B-1}{1-B}} f''(x)x = 0 \end{aligned} \tag{11}$$

According to Yang and Huang (2013), $f'(x)$ can be derived from Eq. (11) on the basis of the variation method of constants.

$$f'(x) = \left(\frac{\gamma}{2k}x + \frac{c_0}{x}\right)^{\frac{1-B}{B}} \tag{12}$$

where $k = \frac{1}{B}\sigma_{ci}(AB)^{\frac{1}{1-B}}$ and $c_0$ is an integration constant. It is worth emphasizing that the primary objective of this study is to rigorously derive equation $f(x)$. However, Eq. (12) is a nonlinear differential equation, and the equation $f(x)$ cannot be directly solved by the integral calculation method. Fortunately, the parameter B exerts a substantial impact on the solution process of Eq. (12). Clearly, when $B$=0.5, Eq. (12) reduces a linear first-order differential equation that can be obtained by integral calculus, whereas Eq. (12) transforms into a nonlinear first-order differential equation requiring numerical methods for solution, subject to the condition of $B$≠0.5. Therefore, the solution process of Eq. (12) is divided into two steps. First, under the condition of $B$=0.5, Eq. (12) is solved by the analytical method; and second, the numerical method is used to solve Eq. (12) under the condition of $B$≠0.5. When $B$=0.5, Eq. (12) is reduced to the following form

$$f'(x) = \frac{\gamma}{2k}x + \frac{c_0}{x} \tag{13}$$

By utilizing integral calculation, $f(x)$ is calculated as follows

$$f(x) = \frac{\gamma}{2A^2\sigma_{ci}}x^2 + c_0 \ln x + c_1 \tag{14}$$

where $c_1$ is an integration constant. For the purpose of obtaining the final equation of $f(x)$, geometric and stress boundary conditions are required to find out the values of $c_0$ and $c_1$. Based on the rock mass failure mechanism depicted in Fig. , the collapse curves intersect with the karst cave bottom. Thus, the geometric boundary condition is written as

$$\begin{cases} f(L_1) = H + \sqrt{R^2 - L_1^2} \\ f(L_2) = 0 \end{cases} \tag{15}$$

Furthermore, because there is an absence of shear stress distribution along the inner surface of the spherical karst cave, the shear stress of the element at the intersection of the collapse surface and the cave is null. Consequently, the stress boundary condition that satisfies the above condition is

$$\tau_{xz}\left(x = L_1, z = H + \sqrt{R^2 - L_1^2}\right) = 0 \tag{16}$$

By establishing an equilibrium differential equation of the element, the shear stress of the element is obtained:

$$\tau_{xz} = \frac{1}{2}\sigma_n \sin 2\theta - \tau \cos 2\theta \tag{17}$$

where $\theta$ represents the angle between the normal vector of a random point on the collapse surface and the horizontal direction. As $f'(x)$ is the first derivative of the velocity discontinuity curve $f(x)$, $f'(x) = cot\,\theta$. Using trigonometric functions, the relations among sin2$\theta$, cos2$\theta$ and $f'(x)$ are written as:

$$\sin 2\theta = \frac{2f'(x)}{f'(x)^2 + 1} \quad \cos 2\theta = \frac{f'(x)^2 - 1}{f'(x)^2 + 1} \tag{18}$$

Substituting Eqs. (1), (17), and (18) into Eq. (16), the value of $c_0$ is obtained as:

$$c_0 = -\frac{\gamma L_1^2}{A^2\sigma_{ci}} \tag{19}$$

In accordance with the upper bound theorem of limit analysis, the external work rate is equivalent to internal dissipation rate. According to this condition, an equation that can be used to determine the value of $L_1$ is

$$\begin{aligned} &2\pi\int_{L_1}^{L_2}\left\{\sigma_{ci}[ABf'(x)]^{\frac{1}{1-B}}\left(1 - B^{-1}\right) - \sigma_{tm}\right\} xv\mathrm{d}x \\ &-2\pi R\left(R - \sqrt{R^2 - L_1^2}\right)Tv + \pi L_2^2 qv - \pi\gamma v\int_{L_2}^{L_1} x^2 f'(x)\mathrm{d}x \\ &+\pi\gamma v\frac{1}{3}\left(R - \sqrt{R^2 - L_1^2}\right)^2\left(2R + \sqrt{R^2 - L_1^2}\right) = 0 \end{aligned} \tag{20}$$

Combining Eqs. (13), (14), (15), (19) and (20), nonlinear equations related to the unknowns $L_1$, $L_2$ and $c_1$ are derived

$$\begin{cases} \frac{\gamma}{2A^2\sigma_{ci}}L_1^2 + c_0 \ln L_1 + c_1 = H + \sqrt{R^2 - L_1^2} \\ \frac{\gamma}{2A^2\sigma_{ci}}L_2^2 + c_0 \ln L_2 + c_1 = 0 \\ \frac{\gamma^2}{8A^2\sigma_{ci}}\left(L_2^4 - L_1^4\right) + \frac{A^2\sigma_{ci}c_0^2}{2}\left(\ln L_1 - \ln L_2\right) + \sigma_{tm}\left(L_1^2 - L_2^2\right) \\ +\frac{\gamma}{3}\left(R - \sqrt{R^2 - L_1^2}\right)^2\left(2R + \sqrt{R^2 - L_1^2}\right) \\ -2TR\left(R - \sqrt{R^2 - L_1^2}\right) + qL_2^2 = 0 \end{cases} \tag{21}$$

By utilizing the numerical method, the values of $L_1$, $L_2$ and $c_1$ are obtained. Subsequently, substituting said values into Eq. (14), the equation of the collapse curve $f(x)$ under the condition of $B$=0.5 is derived.

### *3.2 The calculation for the collapse surface based on the difference method*

As mentioned above, Eq. (12) cannot be solved by the analytical method under the condition of $B\neq0.5$. Thus, the difference method is introduced here to obtain solutions under this non-specialized parameter condition. The difference method is a numerical method that is widely used to solve ordinary and partial differential equations. The fundamental principle of the difference method can be illustrated as follows: substituting the finite-difference quotient for derivative, a differential equation can be approximately presented by a difference equation. Thus, solving a differential equation can be converted into solving an algebraic equation. Based on the fundamental principle of the difference method, the definition domain of the collapse curve $f(x)$ is divided into a large number of very short line segments $\Delta x$, and the length of each $\Delta x$ approaches zero. Along each $\Delta x$, the derivative of the collapse curve $f(x)$ is replaced by the difference quotient based on a suitable iterative equation, and the collapse curve $f(x)$ is discretized into a difference equation. Obtaining the numerical solution for $f(x)$ involves deriving the coordinate of the collapse curve from its initial coordinate.

Because the $f(x)$ is a continuous function, and the derivative of $f(x)$ can be determined by the following derivation process

$$f'(x)=\lim_{\Delta x\to0}\frac{\Delta f(x)}{\Delta x}=\lim_{\Delta x\to0}\frac{f(x+\Delta x)-f(x)}{\Delta x}=\frac{\mathrm{d}f(x)}{\mathrm{d}x} \tag{22}$$

where $\frac{\mathrm{d}f(x)}{\mathrm{d}x}$ denotes the derivative of the function $f(x)$ relative to variable $x$. The derivative can be converted into a difference quotient by using the following equation

$$\frac{\mathrm{d}f(x)}{\mathrm{d}x}=f'(x)\approx\frac{f(x+\Delta x)-f(x)}{\Delta x}=\frac{\Delta f(x)}{\Delta x} \tag{23}$$

where $\frac{\Delta f(x)}{\Delta x}$ is the difference quotient of $f(x)$. Because the length of $\Delta x$ approaches zero, each microsegment on the curve of $f(x)$ approximates a very short line segment connecting points $\{x(i), f[x(i)]\}$ and $\{x(i+1), f[x(i+1)]\}$, as depicted in Fig.2 . The iterative relationship linking a point on the curve $f(x)$ to its subsequent point can be formulated as:

$$f[x(i+1)]=f[x(i)]+\Delta x\cdot f'[x(i)] \tag{24}$$

The equation for the collapse curve $f(x)$ can be obtained by using the principle of the difference method and a recursive approach from an initial point. Additionally, the upper bound theorem states that the external work rate at each point on the curve $f(x)$ must be equal to the rate of internal dissipation. Thus, a program to calculate the equation of the collapse curve $f(x)$ is developed within the framework of the difference method and the upper bound theorem. The concept of the program can be described as follows.

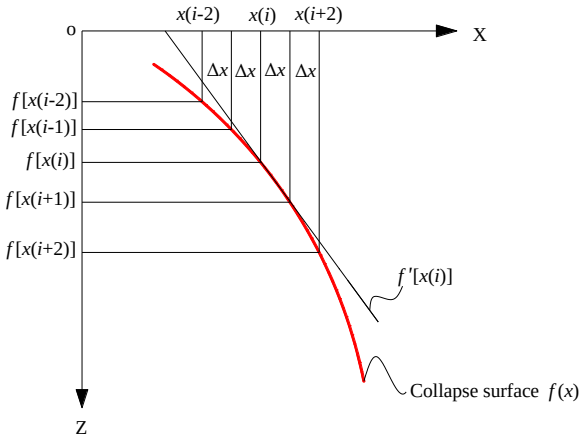


Fig. 2 Principle of the difference method for calculating the collapse surface of rock mass

- First, assuming that the collapse curve $f(x)$ originates from a random point [$L_1$, $f(L_1)$] situated at the spherical karst cave bottom, and terminates at another random point [$L_2$, $f(L_2)$] located on the roof of the excavated cavern, these random points [$L_1$, $f(L_1)$] and [$L_2$, $f(L_2)$] can be regarded as the initial and termination points, respectively, of $f(x)$. Based on Eqs. (8), (12) and (24), a recursive program is written to derive the collapse curve $f(x)$.
- Next, an initial value of $L_1$ is entered into this program, and the program is started. If this $L_1$ value can make the difference between the external work rates and internal dissipation smaller than the tolerance, the program stops. The values of $L_1$ and $L_2$, which correspond to $L_1$, are generated as output. These $L_1$ and $L_2$ values are the upper bound results of the radii of the circular top and bottom surfaces, respectively, of the collapse block.
- If this $L_1$ value cannot decrease the difference between the external work rate and internal dissipation below the tolerance, the previous step is repeated until this difference is smaller than the tolerance.

A diagram of the program concept is shown in Fig. 3.

### *3.3 Comparison of the analytical and numerical solutions for collapse surfaces*

As previously noted, the analytical solution for collapse curve $f(x)$ can be explicitly derived when $B$=0.5, while scenarios involving $B\neq0.5$ require numerical computation of this collapse curve through difference method. However, when $B$=0.5, the numerical solution of $f(x)$ can also be computed via the difference method. To validate the numerical solutions

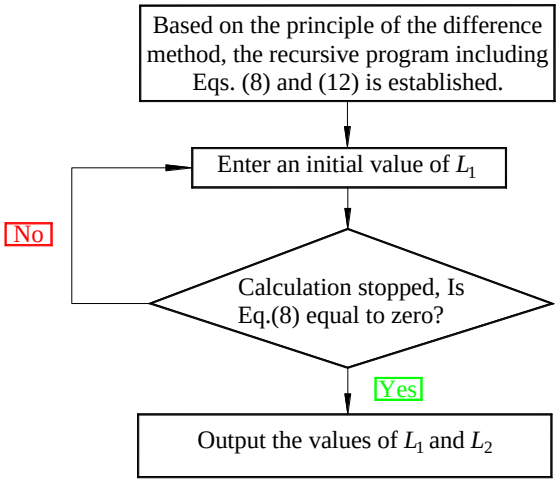


Fig. 3 Calculation diagram of the collapse curve $f(x)$ based on the difference method

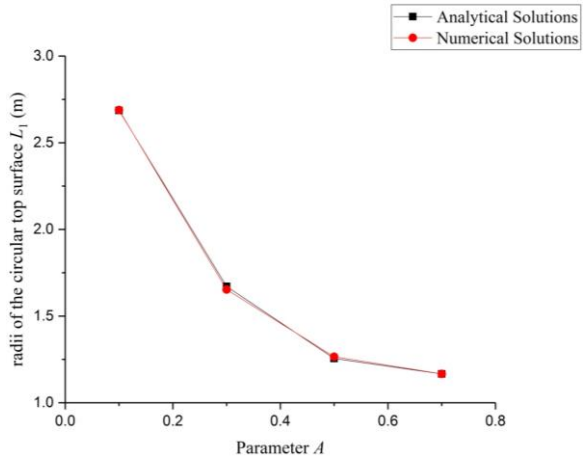


Fig. 4 Comparison of the $L_1$ values between the analytical and numerical solutions

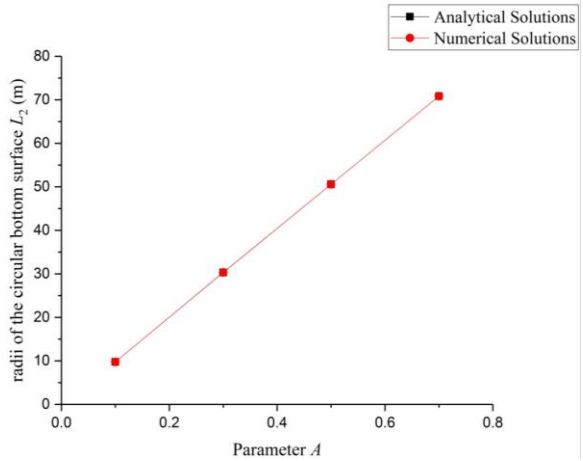


Fig. 5 Comparison of the $L_2$ values between the analytical and numerical solutions

provided by the difference method, the values of $L_1$ and $L_2$ derived from the analytical method were compared with those calculated by the difference method under the condition of $B$=0.5. To visualize the difference between the analytical and difference methods, the values of $L_1$ and $L_2$ obtained from the two methods for $A$=0.1~0.7, $\gamma$ =25kN/m$^3$, $\sigma_{ci}$ =10 MPa, $\sigma_{tm}$ =$\sigma_{ci}$/100, $T$=10 kPa, $q$=20 kPa, $R$=3 m and $H$=10 m are listed in Table 1.

As shown by the data in Table 1 and illustrated in Figs. 4 and 5, the analytical solutions and the difference method exhibit excellent consistency when calculating both $L_1$ and $L_2$. The maximum observed discrepancy between the two methods is notably small, at 1.095% for $L_1$ and only 0.052% for $L_2$. This high level of correlation between the two methods further validates the accuracy of the rock mass collapse surface equation obtained using the difference method.

## 4. Parameter analysis

### *4.1 Analysis of the parameters influence on the shape and range of collapse surface in the rock mass above a deep rectangular cavern*

In order to examine the effect of various parameters on the collapse surface shape and range of rock mass caused by a spherical karst cave situated above the roof of a deep rectangular cavern, the three-dimensional rock mass collapse surface is plotted based on the theoretical calculation for $A$=0.1~0.9, $B$=0.5~0.9, $\gamma$ =21~25 kN/m$^3$, $\sigma_{ci}$ =10 MPa, $\sigma_{tm}$ =$\sigma_{ci}$/130~$\sigma_{ci}$/90, $T$=0~150 kPa, $q$=5~45 kPa, $R$=1~5 m , and $H$=9~13 m, as shown in Figs. 6-13.

Figs. 6-13 demonstrate that the configuration of the collapse surface of the rock mass, caused by the hidden spherical karst cave, takes on the form of a truncated cone. However, in contrast to a true truncated cone, the collapse surface presented here is composed of curves, but the outside surface of a true truncated cone is composed of lines. Furthermore, the parameters $A$, $B$, $\gamma$ , $q$, $\sigma_{tm}$ , $H$, $R$ and $T$ significantly influence the rock mass collapse range.

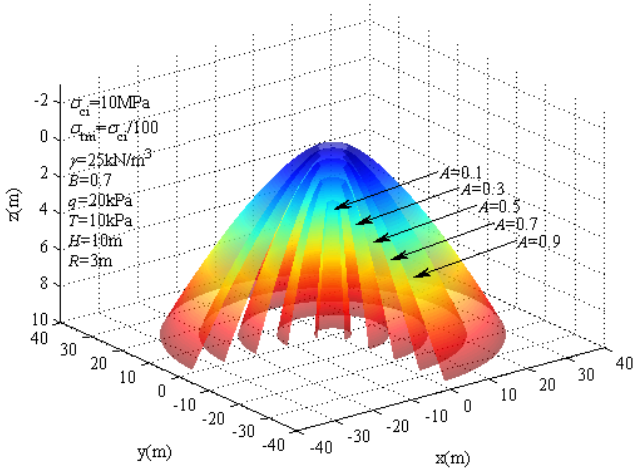


Fig. 6 3D collapse surface caused by a hidden spherical karst cave for various $A$ values

Table 1 Comparisons of the $L_1$ and $L_2$ values between the analytical and numerical solutions under the condition of $B$=0.5

| $A$ | Analytical solutions of $L_1$(m) | Numerical solutions of $L_1$(m) | Difference | Analytical solutions of $L_2$(m) | Numerical solutions of $L_2$(m) | Difference |
|---|---|---|---|---|---|---|
| 0.1 | 2.6859 | 2.6885 | 0.097% | 9.7534 | 9.7585 | 0.052% |
| 0.3 | 1.6713 | 1.6530 | 1.095% | 30.3044 | 30.3130 | 0.028% |
| 0.5 | 1.2552 | 1.2657 | 0.837% | 50.5785 | 50.5757 | 0.006% |
| 0.7 | 1.1662 | 1.1666 | 0.034% | 70.8240 | 70.8266 | 0.004% |

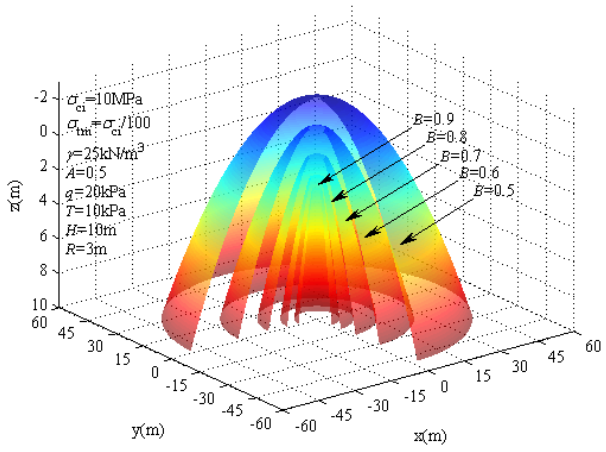


Fig. 7 3D collapse surface caused by a hidden spherical karst cave for various $B$ values

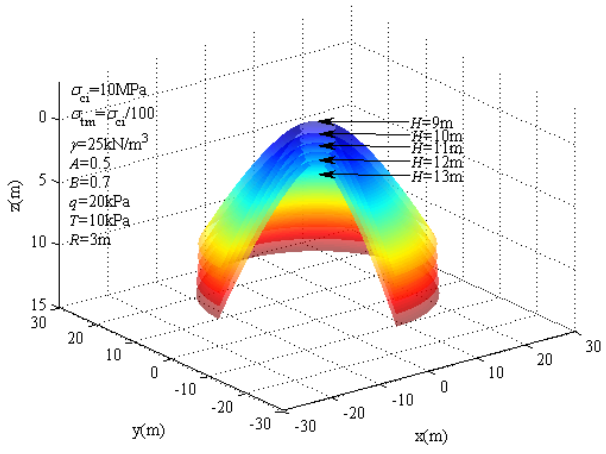


Fig. 8 3D collapse surface caused by a hidden spherical karst cave for various $H$ values

The collapse range of the rock mass enlarged as $A$, $H$, $T$ and $\sigma_{tm}$ increased, conversely, as $B$, $R$, $\gamma$ and $q$ increased, it reduced.

### *4.2 The collapse volume of the rock mass above a deep rectangular cavern caused by a spherical karst cave*

A hidden spherical karst cave above a deep rectangular cavern may cause rock mass collapse during cavern excavation

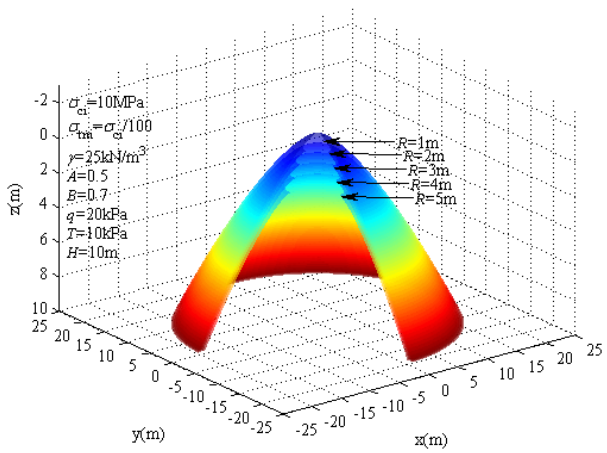


Fig. 9 3D collapse surface caused by a hidden spherical karst cave for various $R$ values

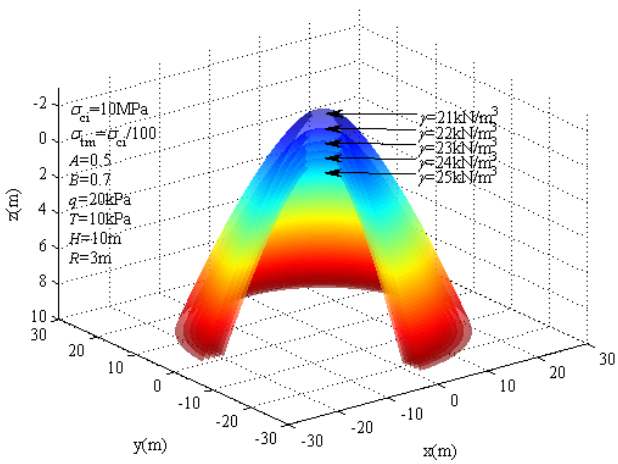


Fig. 10 3D collapse surface caused by a hidden spherical karst cave for various $\gamma$ values

in karst areas. Pouring concrete to backfill the collapsing region is a common treatment method in actual projects. If the rock mass collapse volume can be calculated, the volume of concrete to backfill the collapsing region can be accurately estimated. Consequently, by utilizing the equation that defines the three-dimensional collapse surface of the rock mass, one can obtain the coordinates of points on it. Subsequently, importing these coordinates into the Paint software allows for the precise computation of the volume of rock mass collapse.

Table 2 Rock mass collapse volume above the cavern roof caused by a hidden karst cave for various parameters

| $A$ | $B$ | $H$(m) | $R$(m) | $\gamma$(kN/m$^3$) | $T$(kPa) | $q$(kPa) | $\sigma_{ci}$(MPa) | $\sigma_{tm}$(MPa) | $V$(m$^3$) |
|---|---|---|---|---|---|---|---|---|---|
| 0.1 | 0.7 | 10 | 3 | 25 | 10 | 20 | 10 | $\sigma_{ci}$/100 | 171.5 |
| 0.5 | 0.7 | 10 | 3 | 25 | 10 | 20 | 10 | $\sigma_{ci}$/100 | 5104.8 |
| 0.9 | 0.7 | 10 | 3 | 25 | 10 | 20 | 10 | $\sigma_{ci}$/100 | 17702.1 |
| 0.5 | 0.5 | 10 | 3 | 25 | 10 | 20 | 10 | $\sigma_{ci}$/100 | 51217.5 |
| 0.5 | 0.7 | 10 | 3 | 25 | 10 | 20 | 10 | $\sigma_{ci}$/100 | 5104.8 |
| 0.5 | 0.9 | 10 | 3 | 25 | 10 | 20 | 10 | $\sigma_{ci}$/100 | 567.3 |
| 0.5 | 0.7 | 9 | 3 | 25 | 10 | 20 | 10 | $\sigma_{ci}$/100 | 5035.5 |
| 0.5 | 0.7 | 11 | 3 | 25 | 10 | 20 | 10 | $\sigma_{ci}$/100 | 5249.9 |
| 0.5 | 0.7 | 13 | 3 | 25 | 10 | 20 | 10 | $\sigma_{ci}$/100 | 5556.6 |
| 0.5 | 0.7 | 10 | 1 | 25 | 10 | 20 | 10 | $\sigma_{ci}$/100 | 5653.5 |
| 0.5 | 0.7 | 10 | 3 | 25 | 10 | 20 | 10 | $\sigma_{ci}$/100 | 5104.8 |
| 0.5 | 0.7 | 10 | 5 | 25 | 10 | 20 | 10 | $\sigma_{ci}$/100 | 4293.2 |
| 0.5 | 0.7 | 10 | 3 | 21 | 10 | 20 | 10 | $\sigma_{ci}$/100 | 9227.3 |
| 0.5 | 0.7 | 10 | 3 | 23 | 10 | 20 | 10 | $\sigma_{ci}$/100 | 6608.5 |
| 0.5 | 0.7 | 10 | 3 | 25 | 10 | 20 | 10 | $\sigma_{ci}$/100 | 5104.8 |
| 0.5 | 0.7 | 10 | 3 | 25 | 0 | 20 | 10 | $\sigma_{ci}$/100 | 5051.3 |
| 0.5 | 0.7 | 10 | 3 | 25 | 50 | 20 | 10 | $\sigma_{ci}$/100 | 5344.4 |
| 0.5 | 0.7 | 10 | 3 | 25 | 150 | 20 | 10 | $\sigma_{ci}$/100 | 6056.9 |
| 0.5 | 0.7 | 10 | 3 | 25 | 10 | 5 | 10 | $\sigma_{ci}$/100 | 8174.2 |
| 0.5 | 0.7 | 10 | 3 | 25 | 10 | 25 | 10 | $\sigma_{ci}$/100 | 4393.6 |
| 0.5 | 0.7 | 10 | 3 | 25 | 10 | 45 | 10 | $\sigma_{ci}$/100 | 2254.3 |
| 0.5 | 0.7 | 10 | 3 | 25 | 10 | 20 | 10 | $\sigma_{ci}$/130 | 2438.4 |
| 0.5 | 0.7 | 10 | 3 | 25 | 10 | 20 | 10 | $\sigma_{ci}$/110 | 3900.5 |
| 0.5 | 0.7 | 10 | 3 | 25 | 10 | 20 | 10 | $\sigma_{ci}$/90 | 7131.1 |

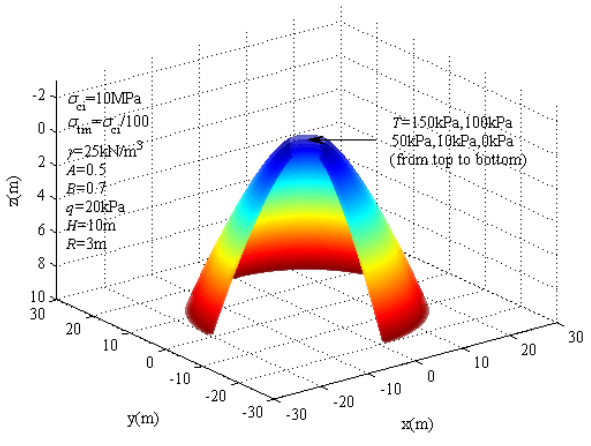


Fig. 11 3D collapse surface caused by a hidden spherical karst cave for various $T$ values

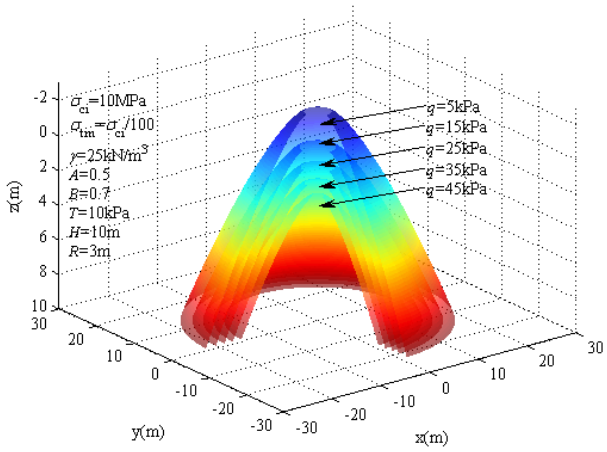


Fig. 12 3D collapse surface caused by a hidden spherical karst cave for various $q$ values

Table 2 summarizes the calculated collapse volume, $V$, of rock mass overlying a deep rectangular cavern induced by a spherical karst cave under varying parameters, to analyze their respective impacts on collapse volume. The results presented in Table 2 demonstrate that the collapse volume shows a positive correlation with parameters $A$, $H$, $T$ and $\sigma_{tm}$, while displaying an inverse relationship with $B$, $R$,

Table 3 Relevant parameters of the numerical model

| Density of rock mass $\gamma$(kN/m$^3$) | Elasticity modulus $E$(GPa) | Poisson's ratio $\mu$ | Compressive strength $\sigma_{ci}$(MPa) | H-B parameter $a$ | H-B parameter $m_b$ | H-B parameter $s$ |
|---|---|---|---|---|---|---|
| 25 | 1.4 | 0.3 | 10 | 0.5 | 3.4954 | 0.035 |

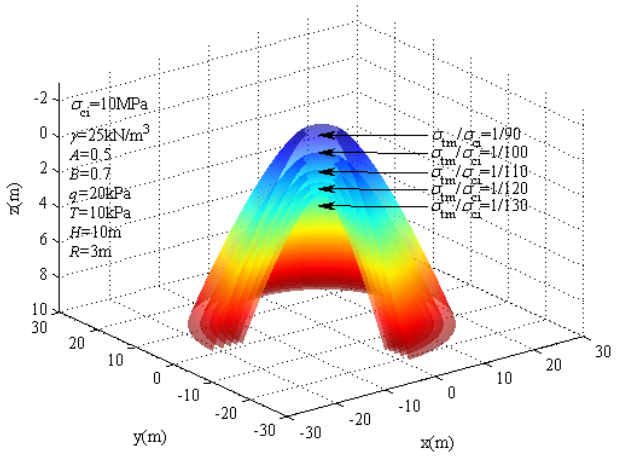


Fig. 13 3D collapse surface caused by a hidden spherical karst cave for various $\sigma_{tm}$ values

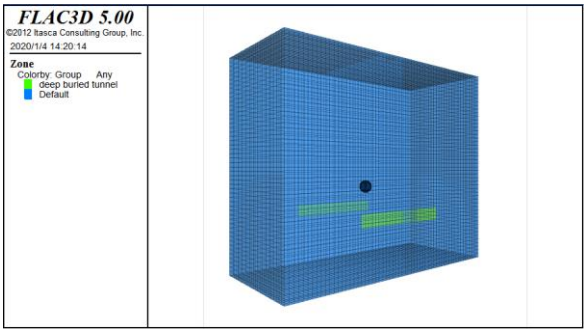


Fig. 14 3D numerical model of a hidden spherical karst cave above a deep rectangular cavern

$\gamma$ and $q$. This parametric analysis reveals that the geomechanical properties of rock mass and the geometric dimensions of cavern significantly influence the magnitude of potential collapses. According to the data contained in Table 2, the rock mass collapse volume can be rapidly determined by geotechnical engineers in practical design applications.

## 5. Comparison of the theoretical and numerical simulation results

### *5.1 Numerical simulation result of the collapse surface caused by a spherical karst cave above a deep rectangular cavern*

In order to evaluate the validity of the theoretical results that have been outlined above, a numerical model in three dimensions is constructed, which describes a spherical karst cave situated above a rectangular cavern, utilizing FLAC3D finite-difference software. By simulating the loosening deformation process of the rectangular cavern roof rock mass during excavation of the rectangular cavern, the rock mass collapse surface shape and range induced by the karst cave are obtained. By comparing the theoretical result with the numerical result under the same conditions, the theoretical result can be verified.

The numerical model consists of a spherical karst cave, a deep rectangular cavern and the surrounding rock mass, as shown in Fig. 14. Because the karst cave in the upper bound calculation is assumed to be a sphere, hence the FISH language generates a cave with a spherical shape in the numerical model. The rectangular cavern and the remaining rock mass are constructed with solid elements. In order to mitigate the impact of the boundary effect on the simulation result, the dimensions of this model are 120, 52 and 100 m in the transverse, longitudinal and vertical directions, respectively. The diameter of the spherical karst cave measures 6 m, and the rectangular cavern roof lies at a distance of 10 m from the cave center. The filler pressure in the karst cave is assumed to be distributed along the radial direction across the cave surface. Moreover, there are 80000 zones and 86278 nodes in this model. The H-B constitutive model in FLAC3D is invoked during the numerical simulation, and the assumed model boundary conditions can be expressed as: the top surface is free, the vertical displacement is fixed at the bottom of the model, and the horizontal displacement is not constrained. Assuming an instantaneous excavation of the rock mass within the rectangular cavern facilitates the excavation process. Moreover, a uniform pressure, simulating the supporting pressure of the cavern lining, is simultaneously exerted on the cavern roof. Refer to Table 3 for the pertinent parameters of this model.

To obtain the rock mass collapse surface shape and range caused by the hidden karst cave, it is crucial to identify an indicator that reflects the rock mass failure surface based on the numerical simulation result. According to the FLAC3D manual (Itasca 2012), the strain rates are nodal zone velocities in the constructed model. Thus, the maximum shear strain rate indicates where plastic flow occurs. For the purposes of printing and plotting, the contour of the maximum shear strain increment is proposed, which is used to illustrate the average strain velocity in the different zones of the model. The contour map of the maximum shear strain increment employs different colors to distinguish different maximum shear strain increments, and the different colors represent the varying degrees of shear failure. Thus, this indicator has been used to define the failure surface by numerous scholars (Karray *et al*. 2018, Zhang *et al*. 2015, Ibrahim *et al*. 2015, Karray *et al*. 2019) in stability analysis in various geotechnical engineering projects. Therefore, this paper also used the

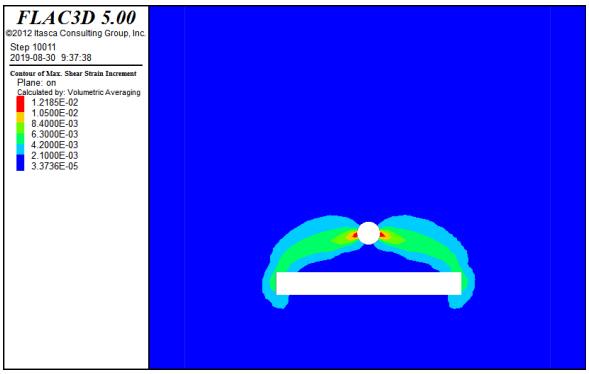


Fig. 15 3D collapse surface of the rock mass offered by the numerical simulation

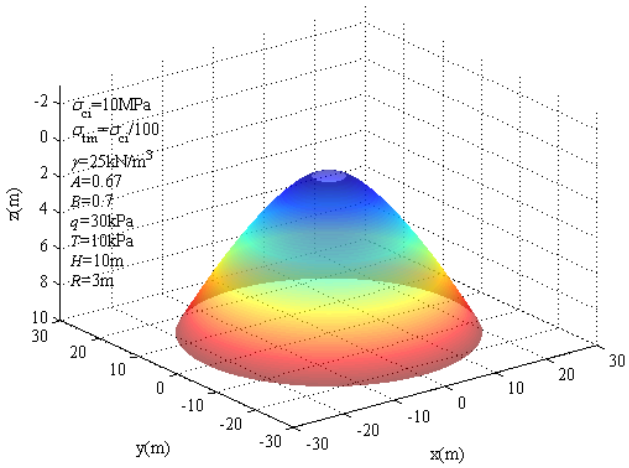


Fig. 16 3D rock mass collapse surface calculated by the kinematic method of upper bound theorem

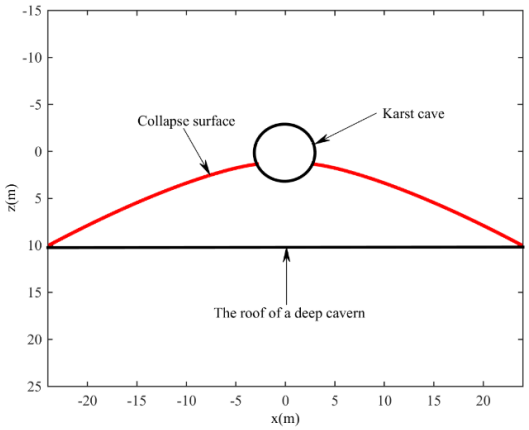


Fig. 17 Projection of theoretical result of the 3D collapse surface onto the XOZ plane

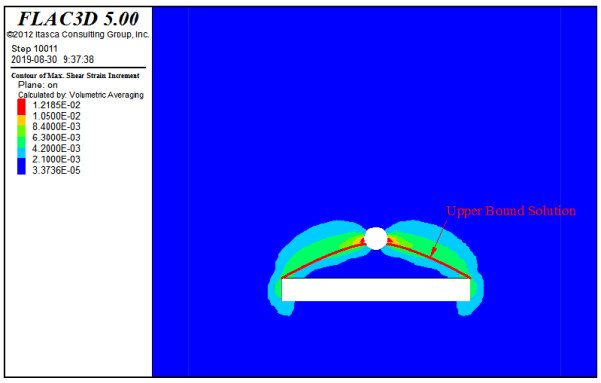


Fig. 18 Comparison of the collapse surfaces calculated by the theoretical method and numerical simulation

maximum shears train increment to define the rock mass collapse surface range caused by the karst cave. Fig. 15 displays a contour map illustrating the maximum shear strain increment across the entire model of the rock mass achieving limit equilibrium state.

Fig. 15 reveals that a shear failure belt appeared between the spherical karst cave and the deep rectangular cavern, extending from the cave bottom to the cavern roof. According to the definition of the maximum shear strain increment, plastic flow occurs along the shear failure belt, and the rock mass surrounded by the shear failure belt may collapse due to superposition of the cave pressure and the self-gravity of the collapse block. The shape, range and position of the shear failure belt, which approximates the result obtained from the theoretical calculation, accurately reflect the characteristics of the rock mass collapse surface.

### *5.2 Comparison of the collapse surfaces between the theoretical analysis and numerical simulation solutions*

Although the shape of the collapse surface obtained from the numerical simulation approximately agrees with the result derived by the theoretical calculation, it is necessary to compare the collapse surfaces derived from the two methods under identical conditions. However, the H-B failure criterion utilized in the theoretical calculation and numerical simulation are of distinct forms, it is imperative to equivalently transform the parameters of both forms of the H-B criterion to enable a comparison under identical conditions. To effectuate this parameter conversion in keeping with the two H-B criterion, Hoek and Brown (1997) introduced a linear regression analysis method, which has been utilized by scholars (Huang *et al*. 2017, Huang *et al*. 2020) to accomplish the above-mentioned equivalent conversion. The H-B parameters, which are equivalent to those listed in Table 3, representing normal and shear stresses are obtained based on the parameter transformation equation introduced by Hoek and Brown (1997). These parameters are summarized in Table 4. Making use of the parameters listed in Table 4 in conjunction with the aforementioned upper bound method, the collapse surface of the rock mass in three dimensions can be observed in Fig. 16. Furthermore, the collapse surface yielded by the numerical simulation is an image in two dimensions that is obtained as the intersection of a profile with the three-dimensional numerical model. Thus, in order to facilitate the comparison between the collapse surface acquired via numerical simulation and the one derived by the upper bound calculation, the three-dimensional collapse surface is intersected by the XOZ plane, as illustrated in Fig. 17. The crimson curves in Fig.

Table 4 Hoek-Brown parameters expressed with the normal and shear stresses form

| Density of rock mass $\gamma$(kN/m$^3$) | Elasticity modulus $E$(GPa) | Poisson's ratio $\mu$ | Compressive strength $\sigma_{ci}$ (MPa) | Tensile strength $\sigma_{tm}$ (MPa) | H-B parameter $A$ | H-B parameter $B$ |
|---|---|---|---|---|---|---|
| 25 | 1.4 | 0.3 | 10 | 0.1 | 0.67 | 0.7 |

17 can be regarded as the projection of the three-dimensional collapse surface onto the XOZ plane. To compare the collapse surfaces calculated by the two methods intuitively, the profile of the collapse mass shown in Fig. 17 is superimposed on Fig. 15, as depicted in Fig. 18. The crimson curves depicted in Fig. 18 delineate the collapse surface calculated by the theoretical calculation. As depicted, the calculated collapse surface of the rock mass, obtained via the upper bound theorem, closely resembles the one obtained via numerical simulation. Consequently, this consistency between the theoretical and numerical collapse surface substantiates the validity of the approach proposed in this paper.

Furthermore, the collapse surface offered by the numerical simulation consists of a shear strain belt whose values are represented by gradually changing shades from light blue to vibrant red. Because plastic flow occurs along the belt, it can be considered that the collapse surface exists within the confines of the belt. Clearly, the rock mass collapse surface yielded from the numerical simulation is an approximate range, and the accuracy of the solution is insufficient. However, the collapse surface yielded through the upper bound calculation comprises two curves, which precisely delineate the collapse surface position and range. Moreover, the collapse volume of the rock mass is also calculated from the theoretical method. Therefore, the collapse surface calculated by the theoretical method is accurate and quantifiable, which may help engineers optimize the construction scheme in an actual project.

## 6. Conclusions

Based on the rock mass collapse characteristic caused by a hidden spherical karst cave situated above the ceiling of a deep rectangular cavern, a three-dimensional rock mass failure mechanism is established. By utilizing this mechanism and the H-B criterion, an analytical equation of the rock mass collapse surface above the deep cavern is derived for the given condition of $B$=0.5, via a variational approach within the domain of the kinematic method of upper bound limit analysis. Furthermore, the rock mass collapse surface for $B \neq 0.5$ is determined via numerical analysis by using the difference method.

In accordance with the collapse surface expression offered by the upper bound calculation, three-dimensional collapse surfaces with various parameters are plotted. The effect of the various parameters on the rock mass collapse range and volume above the cavern roof are investigated. The collapse range and volume of the rock mass exhibited positive correlations with parameters $A$, $H$, $T$ and $\sigma_{tm}$, but demonstrated inverse relationships with parameters $B$, $R$, $\gamma$ and $q$.

By employing finite-difference software FLAC3D, a three-dimensional numerical model that describes a hidden spherical karst cave situated above a deep rectangular cavern is built, and a numerical solution of the rock mass collapse surface caused by the hidden spherical karst cave is obtained. In order to assess the validity of the theoretical solution for the collapse surface in three dimensions, the theoretical and numerical solutions are compared under the identical conditions. The comparison result has demonstrated that the collapse surface shapes and ranges in the theoretical calculation and numerical simulation are virtually identical. Hence, it can be concluded that the presented theoretical method in this study for calculating the collapse surface is indeed valid.

## Acknowledgments

This study was supported by the National Natural Science Foundation of China (Grants No. 52278395 and 51878074), and Research Innovation Project of Changsha university of Science and Technology (Grants No. CX2021BS16). Their financial supports are greatly appreciated.

## References

Caselle, C., Bonetto, S., Comina, C. and Stocco, S. (2020), "GPR surveys for the prevention of karst risk in underground gypsum quarries", *Tunn. Undergr. Sp. Tech.*, **95**, 103137. https://doi.org/10.1016/j.tust.2019.103137.

Chen, W.F. (1975), "*Limit Analysis and Soil Plasticity*", Elsevier Science, Amsterdam, the Netherlands.

FLAC3D Manual; fifth ed.2012; Version 5.0, (2012), Itasca Consulting Group Inc., Minneapolis, MN.

Fraldi, M., Cavuoto, R., Cutolo, A. and Guarracino, F. (2019), "Stability of tunnels according to depth and variability of rock mass parameters", *Int. J. Rock Mech. Min. Sci*., **119**, 222-229. https://doi.org/10.1016/j.ijrmms.2019.05.001.

Fraldi, M. and Guarracino, F. (2009), "Limit analysis of collapse mechanism in cavities and tunnels according to the Hoek-Brown failure criterion", *Int. J. Rock Mech. Min. Sci.*, **46**(4), 665-673. https://doi.org/10.1016/j.ijrmms.2008.09.014.

Fraldi, M. and Guarracino, F. (2010), "Analytical solutions for collapse mechanisms in tunnels with arbitrary cross sections", *Int. J. Solids Struct*., **47**, 216-223. https://doi.org/10.1016/j.ijsolstr.2009.09.028.

Garasic, M. and Garasic, D. (2016), "Some new and interesting caverns in tunnels and along stretches of the Croatian Highways (Dinaric Karst, Croatia)", *Environ. Earth Sci*., **75**, 5. https://doi.org/10.1007/s12665-015-4771-2.

Guan, K., Zhu, W.C., Niu, L.L. and Wang, Q.Y. (2017), "Three-dimensional upper bound limit analysis of supported cavity roof with arbitrary profile in Hoek-Brown rock mass", *Tunn.*

*Undergr. Sp. Tech.*, **69**, 147-154. https://doi.org/10.1016/j.tust.2017.06.016.

He, X.H., Wang, S.M., Lai, M., Peng, X.Y. and Chen, B. (2023), "Mechanical characterization of subway tunnel construction in urban shallow distributed karst stratums", *Transp. Geotech.*, **43**, 101139. https://doi.org/10.1016/j.trgeo.2023.101139.

Hoek, E. and Brown, E.T. (1997), "Practical estimates of the rock mass strength", *Int. J. Rock Mech. Min. Sci.*, **34**(8), 1165-1186. https://doi.org/10.1016/s1365-1609(97)80069-x.

Huang, F., Wang, D., Xiao, N. and Ou, R.C. (2021), "Upper bound limit analysis of blow-out failure mode of excavation face of shield tunnel considering groundwater seepage", *Geomech. Eng.*, **26**(3), 227-234. https://doi.org/10.12989/gae.2021.26.3.227.

Huang, F., Zhang, M., Wang, F., Ling, T.H. and Yang, X.L. (2020), "The failure mechanism of surrounding rock around an existing shield tunnel induced by an adjacent excavation", *Comput. Geotech.*, **117**, 103236. https://doi.org/10.1016/j.compgeo.2019.103236.

Huang, F., Zhao, L.H., Ling, T.H. and Yang, X.L. (2017), "Rock mass collapse mechanism of concealed karst cave beneath deep tunnel", *Int. J. Rock Mech. Min. Sci.*, **91**, 133-138. https://doi.org/10.1016/j.ijrmms.2016.11.017.

Ibrahim, E., Soubra, A.H., Mollon, G., Raphael, W., Dias, D. and Reda, A. (2015), "Three-dimensional face stability analysis of pressurized tunnels driven in a multilayered purely frictional medium", *Tunn. Undergr. Sp. Tech.*, **49**, 18-34. https://doi.org/10.1016/j.tust.2015.04.001.

Karray, M., Hussien, M.N., Delisle, M.C. and Ledoux, C. (2018), "Framework to assess the pseudo-static approach for theseismic stability of clayey slopes", *Can. Geotech. J.*, **55**(12), 1860-1876. https://doi.org/10.1139/cgj-2017-0383.

Karray, M., Hussien, M.N., Souilem, M., Locat, P. and Mompin, R. (2019), "Adjustment of the spectral pseudo-static approach to account for soil plasticity and zone seismicity", *Can. Geotech. J.*, **56**(2), 173-186. https://doi.org/10.1139/cgj-2017-0414.

Li, S.C., Wu, J., Xu, Z.H., Zhou, L. and Zhang, B. (2019), "A possible prediction method to determine the top concealed karst cave based on displacement monitoring during tunnel construction", *Bull. Eng. Geol. Environ.*, **78**, 341-355. https://doi.org/10.1007/s10064-017-1060-1.

Li, T.Z. and Yang, X.L. (2017), "Limit analysis of failure mechanism of tunnel roof collapse considering variable detaching velocity along yield surface", *Int. J. Rock Mech. Min. Sci.*, **100**, 229-237. https://doi.org/10.1016/j.ijrmms.2017.10.028.

Lyu. C. and Zeng, Z.Q. (2019), "Upper bound limit analysis of unsymmetrical progressive collapse of shallow tunnels in inclined rock stratum", *Comput. Geotech.*, **116**, 103199. https://doi.org/10.1016/j.compgeo.2019.103199.

Ma, D., Miao, X.X., Bai, H.B., Huang, J.H., Pu, H., Wu, Y., Zhang, G.M. and Li, J.W. (2016), "Effect of mining on shear sidewall groundwater inrush hazard caused by seepage instability of the penetrated karst collapse pillar", *Nat. Hazards*, **82**, 73-93. https://doi.org/10.1007/s11069-016-2180-9.

Park, D. and Michalowski, R.L. (2019), "Roof stability in deep rock tunnels", *Int. J. Rock Mech. Min. Sci.*, **124**, 104139. https://doi.org/10.1016/j.ijrmms.2019.104139.

Park, D. and Michalowski, R.L. (2020), "Three-dimensional roof collapse analysis in circular tunnels in rock", *Int. J. Rock Mech. Min. Sci.*, **128**, 104275. https://doi.org/10.1016/j.ijrmms.2020.104275.

Peng, J. and Cai, M. (2019), "A cohesion loss model for determining residual strength of intact rocks", *Int. J. Rock Mech. Min. Sci.*, **119**, 131-139. https://doi.org/10.1016/j.ijrmms.2019.03.032.

Qin, C.B., Chian, S.C., Yang, X.L. and Du, D.C. (2015a), "2D and 3D limit analysis of progressive collapse mechanism for deep-buried tunnels under the condition of varying water table", *Int. J. Rock Mech. Min. Sci.* **80**, 255-264. https://doi.org/10.1016/j.ijrmms.2015.09.024.

Qin, C.B., Yang, X.L., Pan, Q.J., Sun, Z.B., Wang, L.L. and Miao, T. (2015b), "Upper bound analysis of progressive failure mechanism of tunnel roofs in partly weathered stratified Hoek-Brown rock masses", *Int. J. Rock Mech. Min. Sci.*, **74**, 157-162. https://doi.org/10.1016/j.ijrmms.2014.10.002.

Wang, H.T., Wang, L.G., Li, S.C., Wang, Q., Liu, P. and Li, X.J. (2019), "Roof collapse mechanisms for a shallow tunnel in two-layer rock strata incorporating the influence of groundwater", *Eng. Fail. Anal.*, **98**, 215-227. https://doi.org/10.1016/j.engfailanal.2019.01.062.

Wu, B., Sun, W.T., Cai, G.W. and Meng, G.W. (2022), "Reliability analysis of shallow-buried tunnel construction adjacent to karst cave", *Comput. Geotech.*, **145**, 104673. https://doi.org/10.1016/j.compgeo.2022.104673.

Wu, J., Li, S.C., Xu, Z.H. and Zhao, J. (2019), "Determination of required rock thickness to resist water and mud inrush from karst caves under earthquake action", *Tunn. Undergr. Sp. Tech.*, **85**, 43-55. https://doi.org/10.1016/j.tust.2018.11.048.

Xiao, Q.F., Li, S.W., Ye, F., Qian, R., Liao, H.Y., Ye, B.S. and Fu, W.X. (2024), "Explicit analytical solution to the minimum safety thickness of waterproof-resistant slab in front of karst tunnel face", *Eng. Fail. Anal.*, **157**, 107941. https://doi.org/10.1016/j.engfailanal.2023.107941.

Xiao, Y., Zhao, M.H., Zhang, R., Zhao, H. and Wu, G.Q. (2019), "Stability of dual square tunnels in rock masses subjected to surcharge loading", *Tunn. Undergr. Sp. Tech.*, **92**, 103037. https://doi.org/10.1016/j.tust.2019.103037

Xu, Z.H., Wu, J., Li, S.C., Zhang, B. and Huang, X. (2018), "Semianalytical solution to determine minimum safety thickness of rock resisting water inrush from filling-type karst caves", *Int. J. Geomech.*, **18**(2), 04017152. https://doi.org/10.1061/(ASCE)GM.1943-5622.0001071

Yang, X.L. and Huang, F. (2013), "Three-dimensional failure mechanism of a rectangular cavity in a Hoek–Brown rock medium", *Int. J. Rock Mech. Min. Sci.*, **61**, 189-195. https://doi.org/10.1016/j.ijrmms.2013.02.014,

Yang, X.L. and Li, K.F. (2016), "Roof collapse of shallow tunnel in layered Hoek-Brown rock media", *Geomech. Eng.*, **11**(6), 867-877. https://doi.org/10.12989/gae.2016.11.6.853,

Yang, X.L., Li, Z.W., Liu, Z.A. and Xiao, H.B. (2017), "Collapse analysis of tunnel floor in karst area based on Hoek-Brown rock media", *J. Cent. South Univ.*, **24**, 957-966. https://doi.org/10.1007/s11771-017-3498-5.

Yang, X.L. and Zhang, R. (2017), "Collapse analysis of shallow tunnel subjected to seepage in layered soils considering joined effects of settlement and dilation", *Geomech. Eng.*, **13**(2), 217-235. https://doi.org/10.12989/gae.2017.13.2.217.

Yang, Z.H. and Zhang, J.H. (2016), "Minimum safe thickness of rock plug in karst tunnel according to upper bound theorem", *J. Cent. South Univ.*, **23**, 2346-2353. https://doi.org/10.1007/s11771-016-3293-8.

Zhang, B., Wang, X., Zhang, J.S. and Meng, F. (2017), "Three-dimensional limit analysis of seismic stability of tunnel faces with quasi-static method", *Geomech. Eng.*, **13**(2), 301-318. https://doi.org/10.12989/gae.2017.13.2.301.

Zhang, K., Cao, P., Meng, J.J., Li, K.H. and Fan, W.C. (2015), "Modeling the progressive failure of jointed rock slope using fracture mechanics and the strength reduction method", *Rock Mech. Rock Eng.*, **48**, 771-785. https://doi.org/10.1007/s00603-014-0605-x.

Zhang, R. (2019), "Catastrophe analysis of deep tunnel above water-filled caves", *J. Cent. South Univ.*, **26**(7), 1820-1829. https://doi.org/10.1007/s11771-019-4136-1.
Zhang, R. and Yang, X.L. (2019), "New 3D failure analysis of water-filled karst cave beneath deep tunnel", *Geomech. Eng.*, **18**(1), 1-9. https://doi.org/10.12989/gae.2019.18.1.001.

*CC*